Current density in Saturn's equatorial current sheet: Cassini magnetometer observations

C. J. Martin[1], **C. S. Arridge**[1]

[1]Physics Department, Lancaster University, Bailrigg, Lancaster, LA1 4YB, United Kingdom.

Key Points:

- Current density is estimated using a deformed Harris current sheet model
- Current density generally decreases with radial distance with some local time asymmetries mainly in the azimuthal current
- Divergence of the perpendicular current density used to infer parallel field aligned currents that can enhance auroral emission pre-midnight

Corresponding author: C. J. Martin , c.martin1@lancaster.ac.uk

Abstract

The equatorial current sheet at Saturn is the result of a rapidly rotating magnetosphere. The sheet itself exhibits periodic seasonal and diurnal movements as well as aperiodic movements of a currently unknown origin, along with periodic thickening and thinning of the magnetodisc, and azimuthal changes in the thickness due to local effects in the magnetosphere. In this paper aperiodic movements of the magnetodisc are utilised to calculate the height integrated current density of the current sheet using a Harris current sheet model deformed by a Gaussian wave function. We find a local time asymmetry in both the radial and azimuthal height integrated current density. We note that the local time relationship with height integrated current density is similar to the relationship seen at Jupiter, where a peak of $\sim 0.04\ Am^{-1}$ at $\sim$ 3 SLT (Saturn Local Time) is seen inside 20 R_S. The divergence of the radial and azimuthal current densities are used to infer the parallel currents, which are seen to diverge from the equator in the pre-noon sector and enter the equator in the pre-midnight sector.

1 Introduction

Saturn's rotationally dominated magnetosphere [*Southwood & Kivelson*, 2001] is home to an equatorial current sheet (the magnetodisc) that is produced, in part, by the centrifugal stresses caused by the fast rotation [*Arridge et al.* [2007], *Kellett et al.* [2009] & *Sergis et al.* [2011]] and the internal plasma sources of the magnetosphere, such as the moon Enceladus and other satellites, the rings and the planet itself [e.g. *Pontius et al.* [2006], *Tokar et al.* [2005], *Jurac et al.* [2002] & *Felici et al.* [2016]] . The current sheet is usually found in all local time sectors of the magnetosphere, except near noon when the magnetosphere is compressed due to solar wind dynamic pressure [*Arridge et al.*, 2008b], and is present outside of $\sim$15 R_S (Saturn radii) where the centrifugal stresses dominate the pressure gradients and magnetic tension forces [*Arridge et al.*, 2007]. The magnetic field at Saturn appears more radially extended than a dipole due to this azimuthal current sheet which is analogous to Jupiter's middle and outer magnetosphere.

The current sheet also shows some radial structure where the magnetic field is affected azimuthally by solar wind compressions and the fast rotation. Where the plasma is sub-corotating the magnetic fields are 'swept-back' at large radial distances, this increases the azimuthal magnetic field component with radial distance. This process is especially prevalent on the dawn flank where confinement of the magnetic field acts with sub-corotation to produce a strongly 'swept-backwards' field. However, on the dusk flank these processes oppose each other, and when confinement of the solar wind is strong and enhanced Chapman-Ferarro currents are present the field can produce a 'swept-forward' field which is pushed forward in the direction of corotation. The dayside magnetosphere may also exhibit swept-forward field during periods of transient solar wind compressions [e.g. *Southwood & Kivelson* [2001] & *Hanlon et al.* [2004]].

Study of the current density in Saturn's magnetodisc can help answer an open question regarding Saturn's magnetosphere: to what extent is Saturn's magnetosphere affected by the solar wind and how does this compare to Earth's solar wind dominated magnetosphere and Jupiter's rotationally dominated magnetosphere? This solar wind interaction at Earth drives field aligned current systems, region 1 and 2 currents, that provide a closing mechanism for ionospheric flows coupling with the magnetosphere. At Jupiter, *Khurana* [2001] argues for the influence of solar wind in the magnetosphere with the existence of regions 1 and region 2 like currents that feed a partial ring current, evident from a large asymmetry in current density in local time, and a solar wind driven convection of magnetic flux. These field aligned currents can be detected by mapping the divergence of the current density in the equatorial region.

This view of Jupiter's equatorial current density is mirrored by magnetohydrodynamic simulations, such as *Walker et al.* [2003] where the current density is weaker on the dayside. Additionally inward radial currents are found in the post noon sector and all along the dusk flank of the magnetosphere. A current pattern similar to the one described in *Khurana* [2001] is also seen in the simulation. *Walker et al.* [2003] also found that when the solar wind dynamic pressure was increased, both the field aligned currents and the current sheet density increased in magnitude.

Current density in Saturn's inner magnetosphere from $5 - 16\ R_S$ has been mapped by *Sergis et al.* [2017] using stress balance in the magnetosphere to calculate the current density. The authors show that hot plasma pressure (hot ions) dominates over the particle pressure (thermal) outside of 12 R_S with various local time effects. The azimuthal current density was shown to have an enhancement from post-noon to midnight compared to the post-midnight to noon sector up to 13 R_S. Outside of 13 R_S the azimuthal current density is larger in the night and dawn sectors compared to the day and dusk sectors. The current density peak was calculated to be $100 - 115\ pA/m^2$ between 7 and 13 R_S. Additionally, *Kellett et al.* [2011] shows the local time variability in the ring current with temporal differences using Cassini's equatorial orbits in 2005 and 2006, where the current is strongest in the dusk to midnight sector with an increase in the morning sector at the studies outer radial limits. Temporally, the current shows a variability of a factor of 2-3 which increases with radial distance. The current density itself is shown to decrease from ~90 pA/m^2 at 9 R_S to ~20 pA/m^2 at 20 R_S. The total ring current at Saturn was discussed using perturbation magnetic fields by *Carbary et al.* [2012a] and calculated to be 9.2 ± 1.0MA in the region of ~3 - 20 R_S where the peak is found at 10 R_S and has a value of ~75 pA/m^2.

The magnetodisc is also thought to periodically thicken, thin and move with a period of close to the planetary period oscillations [*Arridge et al.* [2011], *Provan et al.* [2012]] & *Thomsen et al.* [2016]]. The thickness of the magnetodisc is also variable with local time, the current sheet in the dusk region of giant planet magnetospheres is expected to be thicker due to ambipolar electric fields and/or a more dipolar field [*Krupp et al.* [1999], *Southwood & Kivelson* [2001], *Kellett et al.* [2009], *Arridge et al.* [2015] & *Jia & Kivelson* [2016]]. This was shown in *Martin & Arridge* [2017] where the current sheet scale height was larger in the dusk region. The scale height of the current sheet is also believed to increase with radial distance [e.g. *Vasyliunas*, 1983; *Khurana and Kivelson*, 1989], with this in mind we examine the height integrated current density of the current sheet and its divergence, using parameters derived from *Martin & Arridge* [2017].

The following sections are laid out as follows: section 2 gives an overview of the local current sheet model that the current densities are calculated from, and how the magnetometer data is fitted to the model. Section 3 shows how height integrated current density is calculated from the values given by using the local model. Section 4 shows the spatial and temporal results of the height integrated current density calculations and finally, a discussion and comparison of current density at Jupiter and Earth.

2 Local current sheet model

Aperiodic waves that disturb the current sheet [*Martin & Arridge*, 2017] are utilised to calculate the current density of the current sheet as the waves cause the current sheet to pass over Cassini twice during each event. Aperiodic waves are found in all sectors of the magnetosphere where the current sheet exists and are detected using Cassini's onboard magnetometer [*Dougherty et al.*, 2004] data at a frequency of 1 Hz. An aperiodic wave has a distinct signature in magnetometer data where (in spherical Kronian radial, theta, phi components) the radial and azimuthal components show an anti-phase relationship due to swept-backwards fields. Cassini will first sample the lobe of the magnetosphere, and as the wave passes the spacecraft will sample the current sheet, the opposing lobe if the wave has sufficient amplitude, the current sheet again and finally the starting lobe.

We select field perturbations that have a time period much smaller than the global flapping motions; are unrelated to the seasonal bowl-shape of the current sheet [*Arridge et al.*, 2008a]; do not repeat; and show a deflection of over 1 nT in the radial magnetic field. Additionally, each event must occur inside the magnetopause position which is found by examining the magnetic field data. A total of 1461 events fit these criteria between January 2005 to December 2012 on all equatorial revolutions of Cassini.

To model a wave travelling along a magnetodisc we first start with a modified Harris current sheet as a basis for the local model of the current sheet [*Harris*, 1962]. As this is a local model we can impose a Cartesian coordinate system where $\hat{\boldsymbol{x}}$ is approximately radially outwards from Saturn, $\hat{\boldsymbol{y}}$ is in the direction of corotation and $\hat{\boldsymbol{z}}$ is positive northwards. The stationary current sheet equations are as follows:

$$B_x = B_{x0} \tanh\left(\frac{z - z_0}{H_x}\right), \tag{1}$$

$$B_y = B_{y0} \tanh\left(\frac{z - z_0}{H_y}\right), \tag{2}$$

$$B_z = B_{z0}, \tag{3}$$

where B_{x0}, B_{y0} and B_{z0} are the magnetic field components within the lobes of Saturn's magnetosphere, z_0 is the offset of the centre of the current sheet from $z = 0$ caused by periodic movements of the current sheet and the seasonal bowl shape. Additionally, the Harris current sheet model includes the scale heights, H_x and H_y, of the current sheet in the magnetic field.

To add an aperiodic movement to the current sheet, we propagate a Gaussian wave pulse along the modified Harris current sheet. The Gaussian wave pulse used is as follows:

$$z = A \exp\left[-(\mathbf{k} \cdot \mathbf{r} + \mathbf{k} \cdot \mathbf{u}t - \omega t - \Phi_0)^2\right], \tag{4}$$

where A is the amplitude of the wave, $\mathbf{k}$ is the wave vector, $\mathbf{k} \cdot \mathbf{u}t$ is the doppler shift due to the movement of plasma, ω is the wave frequency and Φ_0 is the phase. A more thorough discussion of this wave function and others investigated can be found in *Martin & Arridge* [2017].

To deform the modified Harris current sheet by the Gaussian wave function, we use the general deformation procedure described within *Tsyganenko* [1998]. Extraction of variables relating to the current sheet and the wave itself are found by fitting the magnetometer data from Cassini to the model described above.

This study is focussed on the current density of the current sheet during the passage of an aperiodic wave and to calculate the current density, we concentrate on the current sheet variables ($B_{x0}, B_{z0}, H_x, H_y, z_0$). For a discussion on the wave properties ($\omega, \boldsymbol{k}$ and A) we refer the reader to *Martin & Arridge* [2017].

Locally, J_y is equivalent to the azimuthal direction, and will be considered an azimuthal component of current density when viewing the magnetosphere as a whole and so will be renamed to J_ϕ in the following sections. Correspondingly, J_x is equivalent to the radial component of the current density and will be renamed to J_r. All further references to currents or 'HICD' in Saturn's magnetosphere describe the height integrated current density.

3 Calculating Height Integrated Current Density

The HICD is calculated using Ampere's Law and following the method laid out within *Khurana* [2001]. Beginning with expressions for the radial and azimuthal current components (5) & (6) and the assumptions of (1) a thin current sheet ($j_z B_\phi << j_\phi B_z$) [*Vasyliunas*, 1983] and (2) a weak dependence of B_{z0} with local time which was tested by plotting B_{z0} vs. SLT for discrete radial distances where a linear fit to the data shows no significant gradients in the data. Using the two assumptions, we can integrate over the height of the current sheet to retrieve equations (7) & (8).

$$J_r = \frac{1}{\mu_0}\Big(\frac{\partial \Delta B_z}{\partial \phi} - \frac{\partial \Delta B_\phi}{\partial z}\Big), \tag{5}$$

$$J_\phi = \frac{1}{\mu_0}\Big(\frac{\partial \Delta B_r}{\partial z} - \frac{\partial \Delta B_z}{\partial r}\Big), \tag{6}$$

$$J'_r = \int J_r \, \mathrm{d}z = -\frac{2B_{\phi 0}}{\mu_0}, \tag{7}$$

$$J'_\phi = \int J_\phi \, \mathrm{d}z = \frac{1}{\mu_0}\Big[2B_{r0} - 2H\frac{\partial B_{z0}}{\partial r}\Big], \tag{8}$$

where ΔB_ϕ and ΔB_r denote the 'differenced' field which has Saturn's dipole removed. The model described in the previous section implements a thin current sheet assumption without the dipole field of Saturn and hence the values $B_{\phi 0}$ and B_{r0} are already considered to be 'differenced'. H is the scale height of the current sheet which is the geometric mean of H_ϕ and H_r. H is used rather than the separate scale heights as they are usually within uncertainties of each other.

To estimate $\frac{\partial \Delta B_z}{\partial r}$ we examine the distribution of B_{z0} with radial distance (fig 1) and fitted its variation with a polynomial: $B_{z0} = \frac{a}{r} + \frac{b}{r^2} + \frac{c}{r^3}$, where $a = 216 \pm 38 \; nT \; R_S$, $b = 6364 \pm 498 \; nT \; R_S^2$, $c = 56410 \pm 2911 \; nT \; R_S^3$. This function is then differentiated and used to calculate J'_ϕ (equation 9).

$$J'_\phi = \int J_\phi \, \mathrm{d}z = \frac{1}{\mu_0}\left[2B_{r0} - 2H\left(\frac{216}{r^2} + \frac{2(6364)}{r^3} + \frac{3(56410)}{r^4}\right)\right], \tag{9}$$

4 Results

4.1 Height Integrated Current Density

Figures 2 and 3 show results for the radial and azimuthal height integrated current density on a logarithmic scale, respectively. Figures 2a and 3a show the HICD as a function of local time. The coloured squares show the average current density within 1 R_S bins projected onto the X-Y plane in KSM (Kronocentric Solar Magnetospheric) coordinates where X is along the Saturn-Sun line, the X-Z plane contains the planetary dipole axis and Y completes the right handed system. Additionally, an approximate range of magnetopause positions calculated from *Arridge et al.* [2006] are shown along with the orbits of Titan at 20 R_S and Rhea at 9 R_S. Parts (b) - (e) show the radial structure of the height integrated current density in separate local time sectors. The sectors are noon (09-15 SLT), morning (03-09 SLT), night (21-03 SLT) and evening (15-21 SLT). The values in parts (b) - (e) are coloured by time of measurement so a comparison between spatial and temporal differences can be understood. Early Cassini revolutions are coloured blue (2005) and later revolutions are orange/yellow in colour (2012). A solid black line is fitted to plots (b) - (e) if a correlation coefficient of > 0.25 is found with radial distance. Additionally, figure 4 shows the values of radial height integrated current density with a diverging scale to emphasise the local time differences in positive and negative values, whereas figure 2a shows the magnitude of the current density.

Uncertainties in these values are extracted from the covariance matrix output of the non-linear least squares fitting, where the square roots of the diagonal elements are the standard deviation of the fitted parameters. A successful fit gives percentage uncertainties of between 1 and 5 % for current sheet properties used in the model, these uncertainties are then propagated using the general method of propagation of errors through to give an uncertainty on the current densities. The percentage uncertainties are directly correlated to the χ^2 value of the goodness of fit, and so if the model fits to a poor degree of goodness then the uncertainties in the value of current density will be larger. The χ^2 value is therefore affected by the suitability of the assumptions considered. *Martin & Arridge* [2017] showed that the scale height of the magnetic field in the current sheet increases with radial distance, and is thicker on the dusk flank. As the model assumes a thin current sheet, we therefore comment that these areas may not adhere completely to the thin current sheet approximation and may differ from the model fitted to events in these areas.

The total current can be calculated by radially integrating the values of radial and azimuthal current density. We additionally split into 6 hour SLT bins to resolve the local time differences in the total current. When integrating radially, we find that we have uneven sampling of events in each 1 R_S radial bin, to resolve this problem we stratify the data in each radial bin by sampling 20 events within each bin with replacement. Each bin with 20 values is then averaged to give one value per radial bin, all radial bins from 10-61 R_S are then summed to give a value of total current. This process is repeated 1000 times to gain a mean and standard deviation for each total current value, these values are presented in table 1.

Local Time		Radial Current [MA]	Azimuthal Current [MA]
All SLT		15.4 ± 4.4	32.8 ± 5.5
Morning	$3 \leq$ SLT < 9	23.3 ± 3.2	34.0 ± 4.8
Noon	$9 \leq$ SLT < 15	4.7 ± 1.5	13.7 ± 2.1
Evening	$15 \leq$ SLT < 21	7.7 ± 2.8	20.1 ± 2.7
Night	$21 \leq$ SLT < 3	20.3 ± 1.7	35.8 ± 2.7

Table 1. Table showing average total current for all local time sectors and total current for each individual 6 hour local time sector.

4.2 Divergence of Height Integrated Current Density

Additionally, the divergence of the HICD in the radial and azimuthal direction can be used to infer the divergence of the perpendicular HICD, which in turn can be used to estimate the field aligned currents using the continuity of currents equation:

$$\nabla \cdot \mathbf{J}_{\perp} = -B \frac{\partial}{\partial l}\left(\frac{J_{\parallel}}{B}\right), \tag{10}$$

where l is a length along the field which is positive towards North and $J_{\parallel}$ is the magnitude of field-aligned current. If equation 10 is integrated over the current sheet thickness, we find:

$$\nabla \cdot (\mathbf{J}'_{\mathbf{r}} + \mathbf{J}'_{\phi}) = \nabla \cdot \mathbf{J}'_{\mathbf{r}} + \nabla \cdot \mathbf{J}'_{\phi} = -2J_{\parallel}\frac{B_z}{B_{lobe}}, \tag{11}$$

where $\frac{B_z}{B_{lobe}}$ is the ratio of the normal field in the current sheet (where $B_z \approx \boldsymbol{B}$ in the current sheet center) to the field strength in the lobe just outside of the current sheet with the assumption that B_z is invariant over the current sheet thickness. The divergence in each of the plots is calculated by binning the values of HICD into 2 R_S bin in radius and 3 SLT bins in azimuth. The gradient in radius (for the radial HICD) and in azimuth (for the azimuthal HICD) are calculated by finding the central differences ($\nabla \cdot \mathbf{J'_r} \sim \frac{J_r^{i+1} - J_r^{i-1}}{2\Delta r}$) in radius and azimuth respectively. Perpendicular divergence is found by adding the divergence of the radial HICD to the divergence of the azimuthal HICD, as described in equation 11.

Figures 5 (a), (c) and (e) show the radial, azimuthal and perpendicular divergence of HICD in Saturn's magnetosphere. Uncertainty plots can be found in figures 5 (b),(d) and (f). For reference, the number of events in each bin can be found in figure 5 (g). All of the figures also show the orbits of Rhea (8 R_S) and Titan (20 R_S) along with a range of magnetopause position using the *Arridge et al.* [2006] magnetopause model. The uncertainty of each binned value is calculated via a bootstrapping method, where the distribution of each bin is sampled with replacement and a distribution of the average value is obtained. The standard deviation of this distribution is the uncertainty value for each bin.

5 Discussion

The radial HICD (figure 2a) decreases with increasing distance from Saturn in all local time sectors. On average, the radial HICD is smallest in the noon sector, and a large asymmetry is seen between dusk and dawn, where at dawn large positive values of radial HICD are found, but either smaller positive or negative values are found in the dusk sector. These negative values are attributed to inward current which is coupled with the swept forward field lines in the dusk sector. The negative values can be seen in figure 4 with a diverging colour bar to accentuate the polarity of the measurements. We note that swept forward field lines are more prevalent in the later stages of the mission. The epoch at which the measurement took place is shown by the colour of the data point in figures 2 & 3 where blue is early (2005) mission and yellow is late (2012). We can see that the majority of the negative values are also sampled much later in the mission (are yellow/orange).

Kivelson et al. [2002] states that the distance from the equator is a variable which can affect the direction of the azimuthal magnetic field, as higher latitudes may be influenced by an additional current system that closes the magnetospheric current. Following, *Davies et al.* [2017] showed that swept forward fields in the high latitudes are swept forward due to solar wind compressions, and show modulation from planetary period oscillations, and hence we may assume that swept forward field seen at the equator may also be solar wind driven. As the aperiodic waves used to calculate the current density in the sheet are a direct sampling of the current sheet by Cassini, we can assume that this latitudinal effect is not affecting the data.

Temporal variations in the HICD is evident in figures 2 (b) and (e) where Cassini sampled this part of the magnetosphere over the majority of the equatorial revolutions. The noon sector (b) shows events that occurred in early 2005 and 2006 (blue) where the radial HICD is on average higher than events that occurred in late 2011 and 2012 (yellow/orange). However, this could be both a temporal and spacial difference, where the blue events are slightly pre-noon and the yellow events are slightly post-noon, hence within this sector it is difficult to dissect the spacial from the temporal changes in Saturn's magnetosphere. However, the evening sector (e) shows a gradual decrease in radial HICD magnitude from green (2010) to yellow (2012), however in this time period Cassini's revolutions are rotating from post-dusk to pre-dusk and a spacial difference may also be seen.

During the time period of 2005-2012, Saturn moves from northern summer in 2005, to equinox in 2009, to southern summer in 2012. Additionally, the Sun is experiencing decreasing solar activity in the early time period, and increasing solar activity in the latter part. Both of these effects may influence the current density in the current sheet through enhanced solar wind coupling or strong compression events. However, the fact that the current system is shown to close is validation of the assumption that the system is invariant over the time frame of Cassini's mission.

Another notable aspect of figure 2 is that when the temporal difference is small the overall decrease of radial HICD with radius is evident, seen in figure 2 (c) and (d). The azimuthal HICD (figure 3) also shows an overall decrease with radial distance and also shows a slight asymmetry where the dawn sector has a slightly higher value than the dusk sector. This asymmetry is most evident when slices at various radial distances are taken (figures 6 & 7). The asymmetry inside of 20 R_S can be considered similar in magnitude to the asymmetry in the radial HICD, but may be enhanced by the spacial variation and number of events in each SLT bin. As both the radial and azimuthal HICD is increasing at dawn we can assume that the current density magnitude in general is increased in this area, but this may be a temporal change as the dusk revolutions occur five years after the dawn revolutions.

In comparison to Jupiter (Figure 11 of *Khurana* [2001]), we see that this asymmetry is also present and reduces with radial distance. The peak of J_r is found at between 0 and 3

LT, which corresponds to the position of the peak at Saturn too. A comparison to Earth [e.g. *Iijima et al.* [1990]], shows that in a solar wind driven system it stands to reason that this peak is found at 0 LT, is symmetrical around the midnight meridian and the asymmetry from noon to midnight does not damp with radial distance. With an addition of a fast-rotating system we can see this shift from midnight meridian to a local time of ∼ 3 with an evident dawn-dusk asymmetry. Figure 6 shows the radial dependence on the radial HICD. Evident is an asymmetry that decreases with radial distance, that is also present in the azimuthal figure. In contrast to this, at Jupiter (figure 12 in *Khurana* [2001]), we can see that the majority of negative values are found in the larger radius bins and the inner magnetosphere ($< 15\ R_J$) does not appear to exhibit any asymmetry within uncertainties. However, at Earth the asymmetry is evident at all radial distances and does not decrease in magnitude due to the system being controlled by the solar wind and not rotation [*Iijima et al.*, 1990].

Figure 5 shows the divergence of the radial (a), azimuthal (c) and perpendicular (e) HICD along with their respective uncertainties (b,d,f) and an occurence plot (g). The divergence of the radial HICD is mostly below 1 pAm^{-2} with an average uncertainty of ∼10% and shows no radial or azimuthal spacial dependance. The divergence of the azimuthal HICD however, shows a patch of positive divergence pre-midnight inside of 30 R_S and an area of negative divergence pre-noon inside of 30 R_S. The average divergence of the azimuthal HICD is mostly below 2 pAm^{-2} with an average uncertainty of ∼3%. We combine the azimuthal and radial divergence (equation 11) to estimate the parallel field aligned current density entering and leaving the equatorial regions from the ionosphere, shown in figure 5 (e). The yellow-red coloured areas shows current being added to the current sheet and the blue areas show current being taken from the current sheet.

We note that in some areas a ‘striping’ effect shows, notably in the radial divergence at 9-12 SLT, which is caused by a bin with a small number of data points (in this example the blue bin has one data point) of which this one data point gives a negative divergence. However, this also effects both the radial neighbours making them appear larger in the positive direction. This effect is accentuated in the radial divergence component due to the, on average, smaller in magnitude values. Stratified sampling of the data in each bin would smooth the distribution, however it would not effect this example and others like it as the bin lacks enough data to effectively stratify. The striping may also be reduced by using coarser bins, however we use 2 R_S and 3 SLT bins as a balance between reduction of noice and preserving resolution. The results of the study are robust to bin size and position changes.

Hence, in the pre-midnight sector current is being drawn from the ionosphere and electrons are flowing into the ionosphere. In the pre-noon sector current is being added to the ionosphere and hence electrons are flowing away from the ionosphere to the current sheet. Coupled with the total current flowing shown in table 1, we find that the azimuthal current is largest in the night and morning sectors, where current that is added pre-midnight will be adding to the total current flowing around the night side. We then see a decrease in current in the day and evening sectors where the current is being diverted through the ionosphere instead of the dayside current sheet.

Using values from table 1 we can estimate that the current that is "lost" in the azimuthal direction from the noon sector to the night sector is 22.2 ± 5.7 MA. Integrating the parallel current (inferred from $\nabla \cdot \mathbf{J}_\perp$) over the arc from 12-28 R_S between 18 and 21 SLT we can find that the total current in this area that is being diverted from the ionosphere is 23.5 ± 4.1 MA which is comparable to the estimated current diverted from the azimuthal direction. *Khurana and Liu* [2018] show a current of 11 MA and 17 MA in the day and night respectively between 4 and 20 R_S giving an estimate of ~6 MA for the diverted current in this area.

The field aligned current system described above can be assumed to be an analogy to Earth's partial ring current which is driven by a sustained particle pressure increase in the tail of Earth's magnetosphere. As Saturn is not dominantly solar wind driven, a continual enhancement of particle pressure is not expected at midnight, however *Sergis et al.* [2017] shows a pressure gradient in the midnight-dawn sector outside of 10 R_S corresponding to the bright main auroral emission at dawn, which may be driving a current system that could be analogous to region 2 currents in Earth's magnetosphere. This current system would then close in the pre-midnight sector where we find the diverged currents. If this is the case and there is sufficient current then we would expect a response in the auroral signatures.

6 Auroral Intensity

$\nabla . \boldsymbol{J'}_\perp$ in the pre-midnight sector averages at 4.0 x 10^{-11} Am^{-2}, and can be converted to a field aligned current using equation 11, which gives a value of $J_{\parallel CS} = 2.0$ x 10^{-11} Am^{-2}. This then needs to be scaled using the mirror ratio to the ionosphere where we find a peak current of $J_{\parallel I} = 200\ nAm^{-2}$, which can only generate an auroral emission if it is larger than the maximum current density that can be carried by magnetospheric electrons without acceleration along the field lines (J_{th}) given by equation 12 (equation 10 in *Cowley* *et al.* [2004]).

$$J_{th} = eN\left(\frac{W_{th}}{2\pi m_e}\right)^{\frac{1}{2}}, \tag{12}$$

where e is the charge on an electron, N is the number density, W_{th} is the thermal energy equivalent to kT and m_e is the mass of an electron. For average values given by *Cowley et al.* [2004] of N =∼ 0.2 cm^{-3} and a temperature of ∼ 150 eV in the central magnetosphere and N =∼ 0.01 cm^{-3} and a temperature of ∼ 1 keV in the outer magnetosphere, we find a range for J_{th} of ∼ 66 to ∼ 8.5 nAm^{-2}. The average current sheet $J_{\|I}$ is ∼ 20 nAm^{-2} which is less than what can be carried by non-accelerated electrons in the middle magnetosphere and hence will not produce auroral emission. However the values of the peak reaches ∼ 200 nAm^{-2} in the pre-midnight sector (current away from ionosphere) and so requires a field-aligned voltage to accelerate the electrons into the ionosphere.

$$E_{f0} = 2NW_{th}\left(\frac{W_{th}}{2\pi m_e}\right)^{\frac{1}{2}} \tag{13}$$

$$E_f = \frac{E_{f0}}{2}\left[\left(\frac{J_{\|I}}{J_{th}}\right)^2 + 1\right] \tag{14}$$

The electron energy flux for non-accelerated electrons is given by equation 13 (equation 11 of *Cowley et al.* [2004]) and is found to be ∼ 0.004 to ∼ 0.02 mWm^{-2} for the outer and middle magnetosphere respectively, using the parameters given earlier. Equation 14 gives the enhanced electron energy flux for the precipitating electrons [*Knight* , 1973; *Lundin & Sandahl*, 1978] assuming that the ratio of the energy gained by the precipitating electrons to their initial energy is much less than the mirror ratio between the acceleration region and the planet. I.e. the acceleration occurs sufficiently far from the planet such that the magnetospheric electron population can be considered an infinite reservoir of particles.

Ray et al. [2009] & *Ray et al.* [2013] show that the acceleration regions at Jupiter and Saturn occur at high magnetic latitudes due to centrifugal forces which confine the plasma population at the magnetosphere and strong gravitational forces at the ionosphere. Therefore, the full current-voltage and energy flux current density relation [*Lundin & Sandahl*, 1978] should be considered for these systems. However, in Saturn's middle magnetosphere (∼ 9 R_S), the linear approximation to the current-voltage relation is applicable because of the small magnetospheric ambipolar potentials (∼ 30 V) and small acceleration potentials relative to the energy of the thermal electron population [*Ray et al.*, 2013]. Therefore, equations 12-14 are adequate for our study.

Using the values and equations above, we find that E_f can range from ∼ 0.1 − 1.1 mWm^{-2} in the upward current region at pre-midnight which covers the middle to outer magnetosphere. A source brightness in far ultra-violet emission of ~ 10 kR for an electron energy flux of 1 mWm^{-2} can be assumed with an energy efficiency of ~ 15% [*Waite et al.*, 1983; *Rego et al.*, 1994]. We obtain an auroral intensity of $1 - 11$ kR resulting from the upward current region in the dusk-midnight sector.

The maximum of the divergence of HICD from the current sheet is found between 12 and 14 R_S which, using moments from *Burton et al.* [2010] and the *Bunce et al.* [2008] mapping model, relates to an area between 12° and 15° colatitude in the Northern ionosphere with a typical magnetopause position. Hence this emission would be colocated with the average position of the main oval [*Carbary et al.*, 2012b; *Nichols et al.*, 2016]. An enhancement of 2 kR is seen around 18-20 LT in the southern aurora [*Lamy et al.*, 2009] which is also seen in northern IR data [*Badman et al.*, 2012]. However, this peak is not seen in northern UV observations from 2011-2013 [*Nichols et al.*, 2016].

The downward current region at pre-noon would map to a region where the aurora is typically brightest, where the downward current gives an auroral intensity of $0.1 - 1.1$ kR which is small compared to other contributions and as such we do not see a trough in the auroral intensity in this area.

7 Summary

In conclusion, a Gaussian wave pulse was used to deform a modified Harris current sheet model, using the general deformation method [*Tsyganenko*, 1998], to simulate an aperiodic wave passage in magnetometer data. This model is then fitted to the magnetometer data from Cassini's MAG, which allows for the estimation of a number of wave and current sheet properties. The magnetic field in the lobes and the scale height of the current sheet are used to calculate the height integrated current density in Saturn's equatorial current sheet. These values are additionally used to calculate the divergence of current from the equatorial plane. The main findings of this study are:

1) HICD magnitude decreases with radial distance from the planet, but both radial and azimuthal HICD show an asymmetry where the dawn sector has larger magnitude values on average than the dusk sector. This is related to the average direction of azimuthal magnetic field in these sectors, i.e. the swept-forward field at dusk and swept-backward and non-dipolar field at dawn. We additionally see a change in total current flowing around the whole system, with averages of 15.4 ± 4.4 MA flowing radial and 32.8 ± 5.5 MA flowing azimuthally. If we add the azimuthal value of 9.2 MA for the area of 3-20 R_S from *Carbary*

et al. [2012a] we find a total current flowing to be approximately 30.2 ± 4.1 MA taking into account the overlap of the two studies.

2) Inward radial currents in the dusk sector are attributed to swept-forward field lines showing a link with the solar wind. Future work will examine the solar wind conditions using propagation models to give evidence for this link.

3) Divergence of the perpendicular current into the equator pre-midnight and out of the equator at pre-noon show evidence of a current system not unlike Earth's region 2 currents, with a region of current directed down to the ionosphere in the pre-noon sector, and up from the ionosphere post-dusk that could produce an enhancement of the aurora of up to $\sim 11\ kR$ with some independent evidence for this in UV and IR auroral data.

4) In comparison with Jupiter and Earth, Saturn's equatorial current density profile is most like Jupiter, in that they are both rotationally driven environments, but Saturn also shows a number of differences to Jupiter, such that the divergence of the azimuthal current is constrained in much smaller areas and the azimuthal HICD shows a much larger asymmetry in comparison to Jupiter's azimuthal HICD shown in *Khurana* [2001].

Acknowledgments

CJM was funded by a Faculty of Science and Technology studentship from Lancaster University. CSA was funded by a Royal Society Research Fellowship. CJM would like to acknowledge useful discussions and comments from Sarah Badman, Licia Ray, Ben Hall, Alex Bader, Nathan Case and Joe Kinrade. Cassini MAG data used in this study may be obtained from the Planetary Data System (http://pds-ppi.igpp.ucla.edu).

References

Arridge, C.S., Achilleos, N., Dougherty, M.K., Khurana, K.K. and Russell, C.T., (2006). Modeling the size and shape of Saturn's magnetopause with variable dynamic pressure. *Journal of Geophysical Research: Space Physics*, *111*(A11) doi:10.1029/2005JA011574.

Arridge, C. S., Russell, C. T., Khurana, K. K., Achilleos, N., André, N., Rymer, A. M., Dougherty, M. K., Coates, A. J., (2007). Mass of Saturn's magnetodisc: Cassini observations, *Geophysical Research Letters*, *34*(A11), 8779–8789 doi:10.1029/2006GL028921.

Arridge, C.S., Khurana, K.K., Russell, C.T., Southwood, D.J., Achilleos, N., Dougherty, M.K., Coates, A.J. and Leinweber, H.K., (2008a). Warping of Saturn's magnetospheric and magnetotail current sheets, *Journal of Geophysical Research: Space Physics*, *113*(A8), 2156–2202 doi:10.1029/2007JA012963.

Arridge, C.S., Russell, C.T., Khurana, K.K., Achilleos, N., Cowley, S.W.H., Dougherty, M.K., Southwood, D.J. and Bunce, E.J., (2008b). Saturn's magnetodisc current sheet. *Journal of Geophysical Research: Space Physics*, *113*(A4) doi:10.1029/2007JA012540.

Arridge, C. S., André, N., Khurana, K. K., Russell, C. T., Cowley, S. W. H., Provan, G., Andrews, D. J., Jackman, C. M., Coates, A. J., Sittler, E. C., Dougherty, M. K., Young, D. T. (2011) Periodic motion of Saturn's nightside plasma sheet *Journal of Geophysical Research*, *116* doi:10.1029/2011JA016827.

Arridge, C. S., Kane, M. , Sergis, N., Khurana, K. K., Jackman, C. J., (2015) Sources of local time asymmetries in magnetodiscs *Space Science Reviews*, *187*, 301–333.

Badman, S.V., Achilleos, N., Arridge, C.S., Baines, K.H., Brown, R.H., Bunce, E.J., Coates, A.J., Cowley, S.W.H., Dougherty, M.K., Fujimoto, M. and Hospodarsky, G., (2012). Cassini observations of ion and electron beams at Saturn and their relationship to infrared auroral arcs. *Journal of Geophysical Research: Space Physics*, *117*(A1) doi:10.1029/2011JA017222

Bunce, E.J., Arridge, C.S., Cowley, S.W.H. and Dougherty, M.K., 2008. Magnetic field structure of Saturn's dayside magnetosphere and its mapping to the ionosphere: Results from ring current modeling. *Journal of Geophysical Research: Space Physics*, *113*(A2) doi:10.1029/2007JA012538

Burton, M.E., Dougherty, M.K. and Russell, C.T., 2010. Saturn's internal planetary magnetic field. *Geophysical Research Letters*, *37*(24) doi:10.1029/2010GL045148

Carbary, J.F., Achilleos, N. and Arridge, C.S., (2012). Statistical ring current of Saturn. *Journal of Geophysical Research: Space Physics*, *117*(A6) doi:10.1029/2011JA017472

Carbary, J.F., (2012). The morphology of Saturn's ultraviolet aurora. *Journal of Geophysical Research: Space Physics*, *117*(A6) doi:10.1029/2012JA017670

Cowley, S.W.H., Bunce, E.J. and O'Rourke, J.M., (2004). A simple quantitative model of plasma flows and currents in Saturn's polar ionosphere. *Journal of Geophysical Research: Space Physics*, *109*(A5) doi:10.1029/2003JA010375

Davies, E.H., Masters, A., Dougherty, M.K., Hansen, K.C., Coates, A.J. and Hunt, G.J., 2017. Swept Forward Magnetic Field Variability in High Latitude Regions of Saturn's Magnetosphere. *Journal of Geophysical Research: Space Physics*, *122*(12) doi:10.1002/2017JA024419

Dougherty, M.K., Kellock, S., Southwood, D.J., Balogh, A., Smith, E.J., Tsurutani, B.T., Gerlach, B., Glassmeier, K.H., Gleim, F., Russell, C.T. and Erdos, G., Neubauer F. M., Cowley S. W. H., (2004), The Cassini Magnetic Field Investigation, *Space Science Reviews*, *114*(1), 331-383.

Felici, M., Arridge, C.S., Coates, A.J., Badman, S.V., Dougherty, M.K., Jackman, C.M., Kurth, W.S., Melin, H., Mitchell, D.G., Reisenfeld, D.B. and Sergis, N., (2016). Cassini observations of ionospheric plasma in Saturn's magnetotail lobes. *Journal of Geophysical Research: Space Physics*, *121*(1), 338-357.

Hanlon, P.G., Dougherty, M.K., Krupp, N., Hansen, K.C., Crary, F.J., Young, D.T. and Tóth, G., (2004). Dual spacecraft observations of a compression event within the Jovian magnetosphere: Signatures of externally triggered supercorotation?. *Journal of Geophysical Research: Space Physics*, *109*(A9) doi:10.1029/2003JA010116

Harris, E. G., (1962). On a plasma sheath separating regions of oppositely directed magnetic field, *Il Nuovo Cimento (1955-1965)*, *23*(1), 115-121.

Iijima, T., Potemra, T.A. and Zanetti, L.J., 1990. Large scale characteristics of magnetospheric equatorial currents. *Journal of Geophysical Research: Space Physics*, *95*(A2), 991-999.

Jia, X. and Kivelson, M.G., 2016. Dawn-dusk asymmetries in rotating magnetospheres: Lessons from modeling Saturn. *Journal of Geophysical Research: Space Physics*, *121*(2), pp.1413-1424.

Jurac, S., McGrath, M.A., Johnson, R.E., Richardson, J.D., Vasyliunas, V.M. and Eviatar, A., 2002. Saturn: Search for a missing water source. *Geophysical Research Letters*, *29*(24) doi:10.1029/2002GL015855

Kellett, S., Bunce, E. J., Coates, A. J., Cowley, S. W. H., (2009). Thickness of Saturn's ring current determined from north-south Cassini passes through the current layer, *Journal of Geophysical Research*, *114*(A4),doi:10.1029/2008JA013942

Kellett, S., Arridge, C.S., Bunce, E.J., Coates, A.J., Cowley, S.W.H., Dougherty, M.K., Persoon, A.M., Sergis, N. and Wilson, R.J., (2011). Saturn's ring current: Local time dependence and temporal variability. *Journal of Geophysical Research: Space Physics*, *116*(A5) doi:10.1029/2010JA016216

Khurana, K.K., Kivelson, M.G.,(1989). On Jovian Plasma Sheet Structure, *Journal of Geophysical Research*, *94*(A9), 11,791-11,803.

Khurana, K.K. (2001). Influence of solar wind on Jupiter's magnetosphere deduced from currents in the equatorial plane. *Journal of Geophysical Research: Space Physics*, *106*(A11), 25999-26016

Khurana, K.K. and Liu, J., (2018). Current Systems in Planetary Magnetospheres: A Comparative Overview. Electric Currents in Geospace and Beyond, Wiley. 17-41.

Kivelson, M.G., Khurana, K.K. and Walker, R.J., (2002). Sheared magnetic field structure in Jupiter's dusk magnetosphere: Implications for return currents. *Journal of Geophysical Research: Space Physics*, *107*(A7) doi:10.1029/2001JA000251

Knight, S., (1973). Parallel electric fields. *Planetary and Space Science*, *21*(5), pp.741-750.

Krupp, N., Dougherty, M. K., Woch, J., Seidel, R., Keppler, E., (1999). Energetic particles in the duskside Jovian magnetosphere, *Geophysical Research Letters*, *34*(A11), 8779-8789.

Lamy, L., Cecconi, B., Prangé, R., Zarka, P., Nichols, J.D. and Clarke, J.T., (2009). An auroral oval at the footprint of Saturn's kilometric radio sources, colocated with the UV aurorae. *Journal of Geophysical Research: Space Physics*, *114*(A10) doi:10.1029/2009JA014401

Lundin, R. and Sandahl, I., (1978). Some characteristics of the parallel electric field acceleration of electrons over discrete auroral arcs as observed from two rocket flights. *European Sounding Rocket, Balloon and Related Research, with Emphasis on Experiments at High Latitudes* (Vol. 135) p 125-136.

Martin, C. J. and Arridge, C. S., (2017). Cassini observations of aperiodic waves on Saturn's equatorial current sheet. *Journal of Geophysical Research: Space Physics*, *122* doi.org/10.1002/2017JA024293

Nichols, J.D., Badman, S.V., Bunce, E.J., Clarke, J.T., Cowley, S.W.H., Hunt, G.J. and Provan, G., 2016. Saturn's northern auroras as observed using the Hubble Space Telescope. *Icarus*, *263*,17-31

Pontius, D. H., and T. W. Hill., (2006) Enceladus: A significant plasma source for Saturn's magnetosphere. *Journal of Geophysical Research: Space Physics*, *111* (A9) doi:10.1029/2006JA011674

Provan, G., Andrews, D. J., Arridge, C. S., Coates, A. J., Cowley, S. W. H., Cox, G., Dougherty, M. K., Jackman, C. M. (2012). Dual periodicities in planetary-period magnetic field oscillations in Saturn's tail. *Journal of Geophysical Research*, *117* A1 doi:10.1029/2011JA017104

Ray, L.C., Su, Y.J., Ergun, R.E., Delamere, P.A. and Bagenal, F., 2009. Current?voltage relation of a centrifugally confined plasma. *Journal of Geophysical Research: Space Physics*, *114*(A4) doi:10.1029/2008JA013969

Ray, L.C., Galand, M., Delamere, P.A. and Fleshman, B.L., 2013. Current?voltage relation for the Saturnian system. *Journal of Geophysical Research: Space Physics*, *118*(6), pp.3214-3222 doi:10.1002/jgra.50330

Rego, D., Prangé, R. and Gérard, J.C., 1994. Auroral Lyman and H2 bands from the giant planets: 1. Excitation by proton precipitation in the Jovian atmosphere. *Journal of Geophysical Research: Planets*, *99*(E8), 17075-17094

Sergis, N., Arridge, C.S., Krimigis, S.M., Mitchell, D.G., Rymer, A.M., Hamilton, D.C., Krupp, N., Dougherty, M.K. and Coates, A.J., (2011). Dynamics and seasonal variations in Saturn's magnetospheric plasma sheet, as measured by Cassini. *Journal of Geophysical Research: Space Physics*, *116*(A4) doi:10.1029/2010JA016180

Sergis, N., Jackman, C.M., Thomsen, M.F., Krimigis, S.M., Mitchell, D.G., Hamilton, D.C., Dougherty, M.K., Krupp, N., Wilson, RJ. (2017). Radial and local time structure of the Saturnian ring current, revealed by Cassini, *Journal of Geophysical Research: Space Physics*, *122*(2)1803-1815.

Southwood, D.J., Kivelson, M. G., (2001). A new perspective concerning the influence of the solar wind on the Jovian magnetosphere *Journal of Geophysical Research: Space Physics* *106*(A4) doi:10.1029/2000JA000236

Thomsen, M. F., Jackman, C. M., Cowley, S. W. H., Jia, X., Kivelson, M. G. and Provan, G., (2016). 2016. Evidence for Periodic Variations in the Thickness of Saturn's Nightside Plasma Sheet, *Journal of Geophysical Research: Space Physics*, *122*(1), 280-292

Tokar, R.L., Johnson, R.E., Thomsen, M.F., Delapp, D.M., Baragiola, R.A., Francis, M.F., Reisenfeld, D.B., Fish, B.A., Young, D.T., Crary, F.J. and Coates, A.J., 2005. Cassini observations of the thermal plasma in the vicinity of Saturn's main rings and the F and G rings. *Geophysical research letters*, *32*(14) doi:10.1029/2005GL022690

Tsyganenko, N.A., (1998). Modeling of twisted/warped magnetospheric configurations using the general deformation method, *Journal of Geophysical Research: Space Physics*, *103*(A10), 23551-23563.

Vasyliunas, V.M., (1983). Plasma distribution and flow. *Physics of the Jovian magnetosphere*, 395-453.

Waite, J.H., Cravens, T.E., Kozyra, J., Nagy, A.F., Atreya, S.K. and Chen, R.H., 1983. Electron precipitation and related aeronomy of the Jovian thermosphere and ionosphere. *Journal of Geophysical Research: Space Physics*, *88*(A8), 6143-6163

Walker, R.J. and Ogino, T., 2003. A simulation study of currents in the Jovian magnetosphere. *Planetary and Space Science*, *51*(4), 295-307.

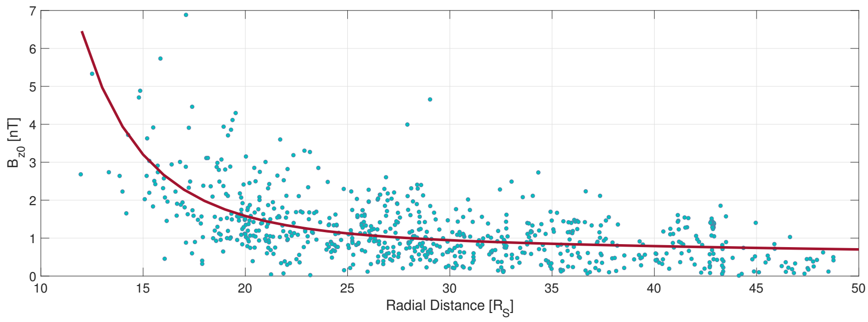

Figure 1. Figure showing measured values of B_{z0} against radial distance (blue dots) fitted with a polynomial (red line)

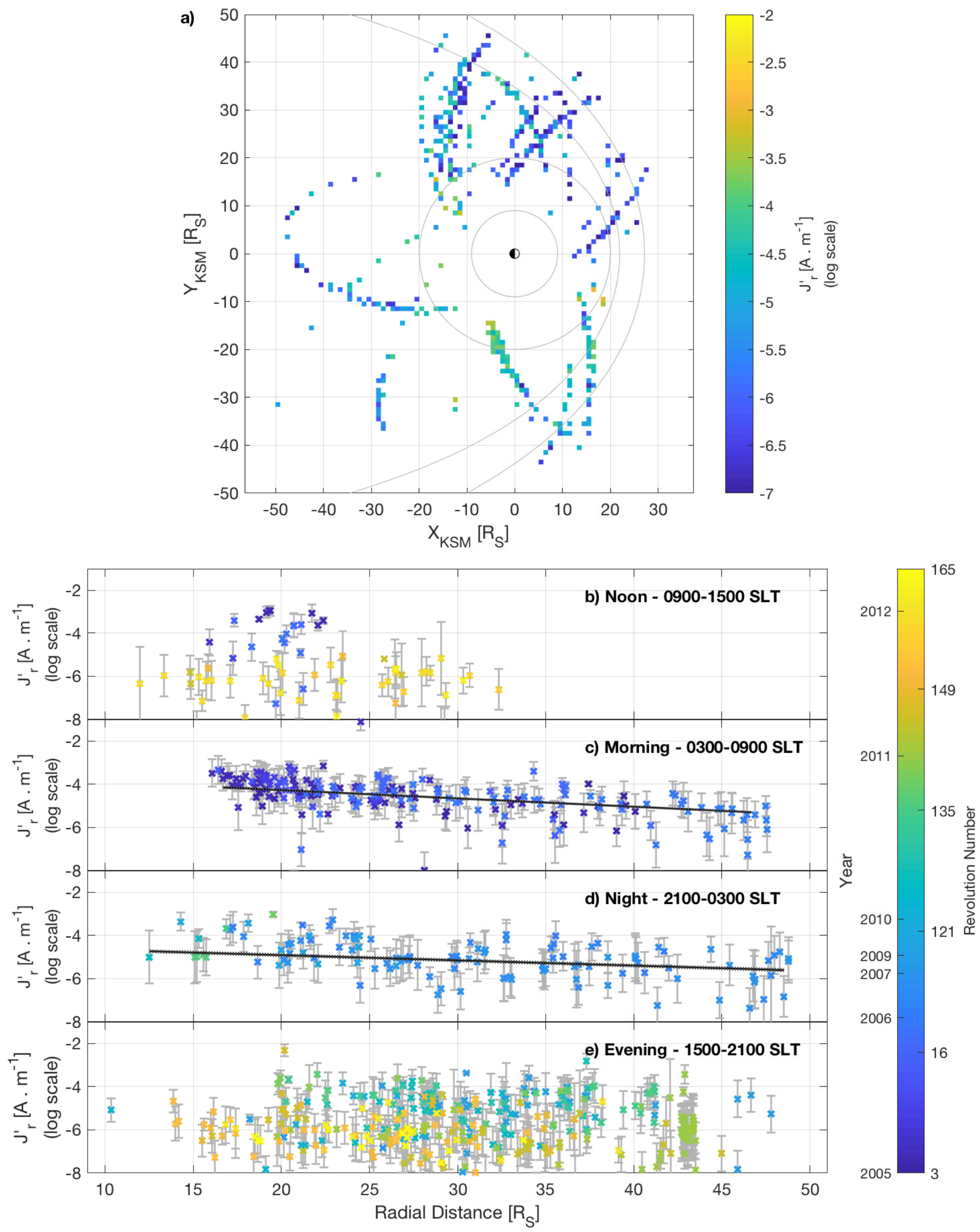

Figure 2. Figure showing the spacial and temporal differences of the radial height integrated current density in Saturn's magnetosphere, plotted on a base 10 logarithmic scale. (a) shows a overview of the entire magnetosphere. The coloured squares show the average value of current density within 1 R_S bins projected onto the X-Y plane in KSM (Kronocentric Solar Magnetospheric) coordinates. Additionally, an approximate range of magnetopause position calculated from *Arridge et al.* [2006] along with the orbits of Titan at 20 R_S and Rhea at 9 R_S are shown by the grey lines. Parts (b) - (e) show the radial structure of the height integrated current density in separate local time sectors coloured by time of measurements.

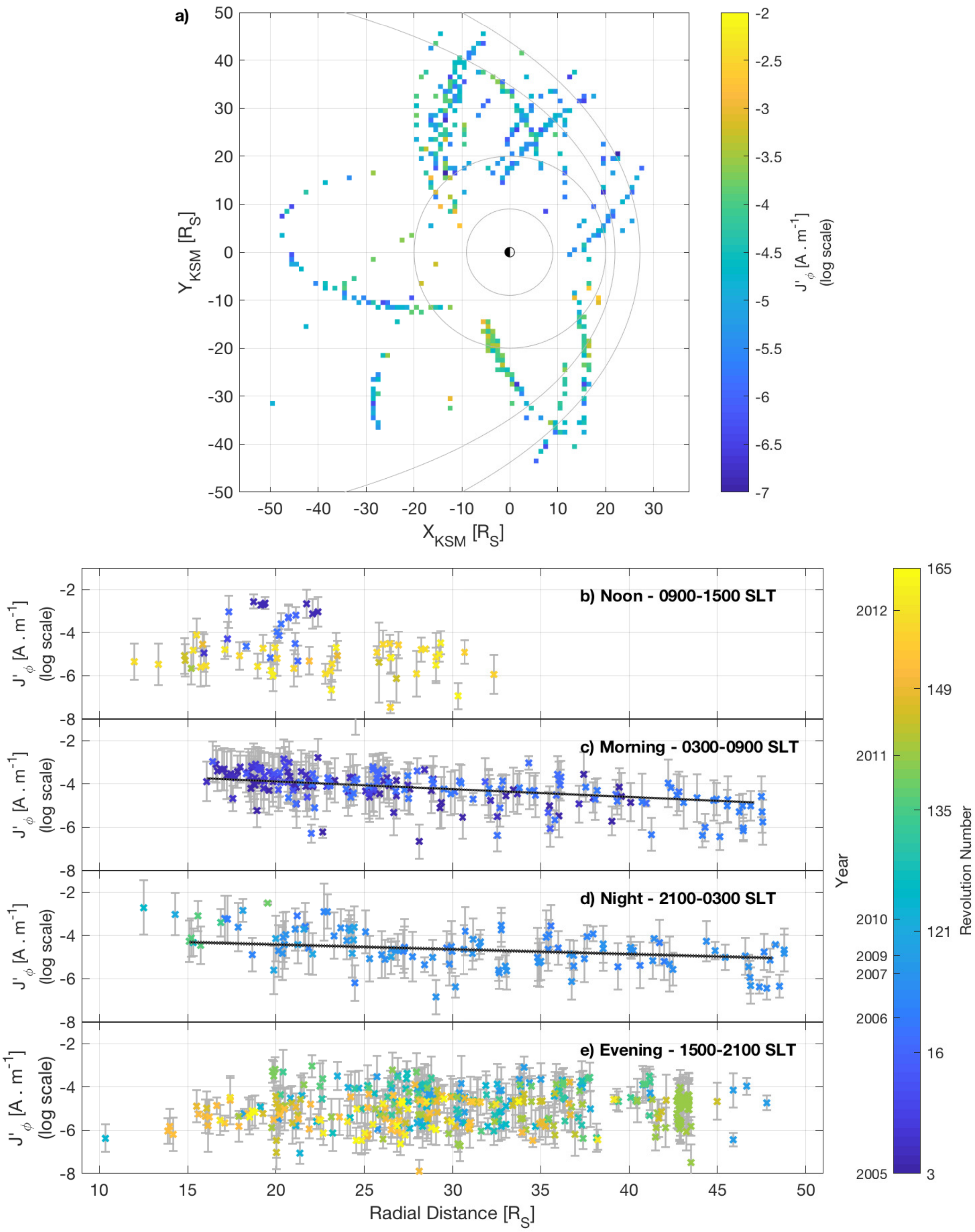

Figure 3. Figure showing the spacial and temporal differences of azimuthal height integrated current density in Saturn's magnetosphere. The figure is int he same format as fig.2.

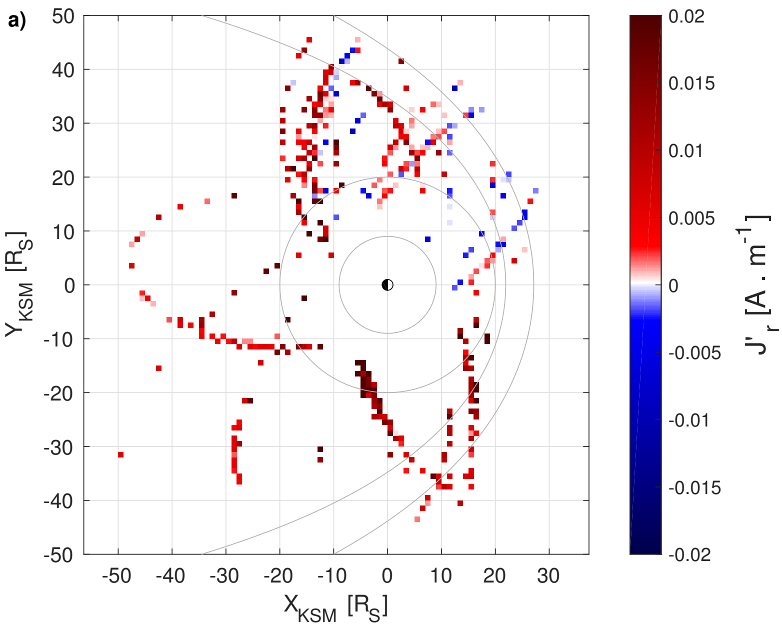

Figure 4. Figure showing the values of height integrated current density with a diverging scale to accentuate the positive and negative radial currents. The coloured squares show the average value of current density within 1 R_S bins projected onto the X-Y plane in KSM (Kronocentric Solar Magnetospheric) coordinates. Additionally, an approximate range of magnetopause position calculated from *Arridge et al.* [2006] along with the orbits of Titan at 20 R_S and Rhea at 9 R_S.

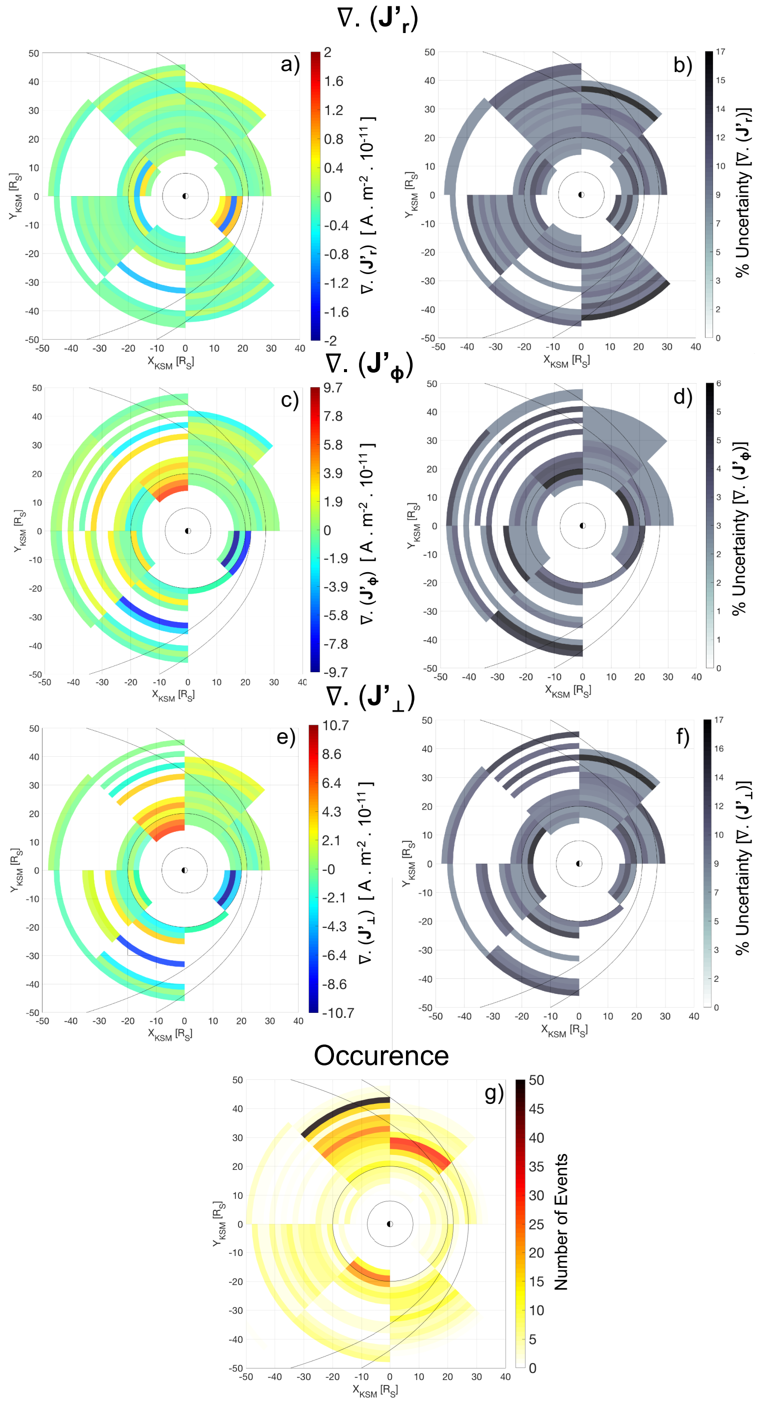

247 **Figure 5.** Figure showing the divergence of height integrated current density. The coloured blocks show the average value of the divergence of height integrated current density projected onto the X-Y plane in KSM coordinates. Additionally, an approximate minimum and maximum magnetopause position calculated from *Arridge et al.* [2006] along with the orbits of Titan at 20 R_S and Rhea at 9 R_S are indicated by the curved lines.

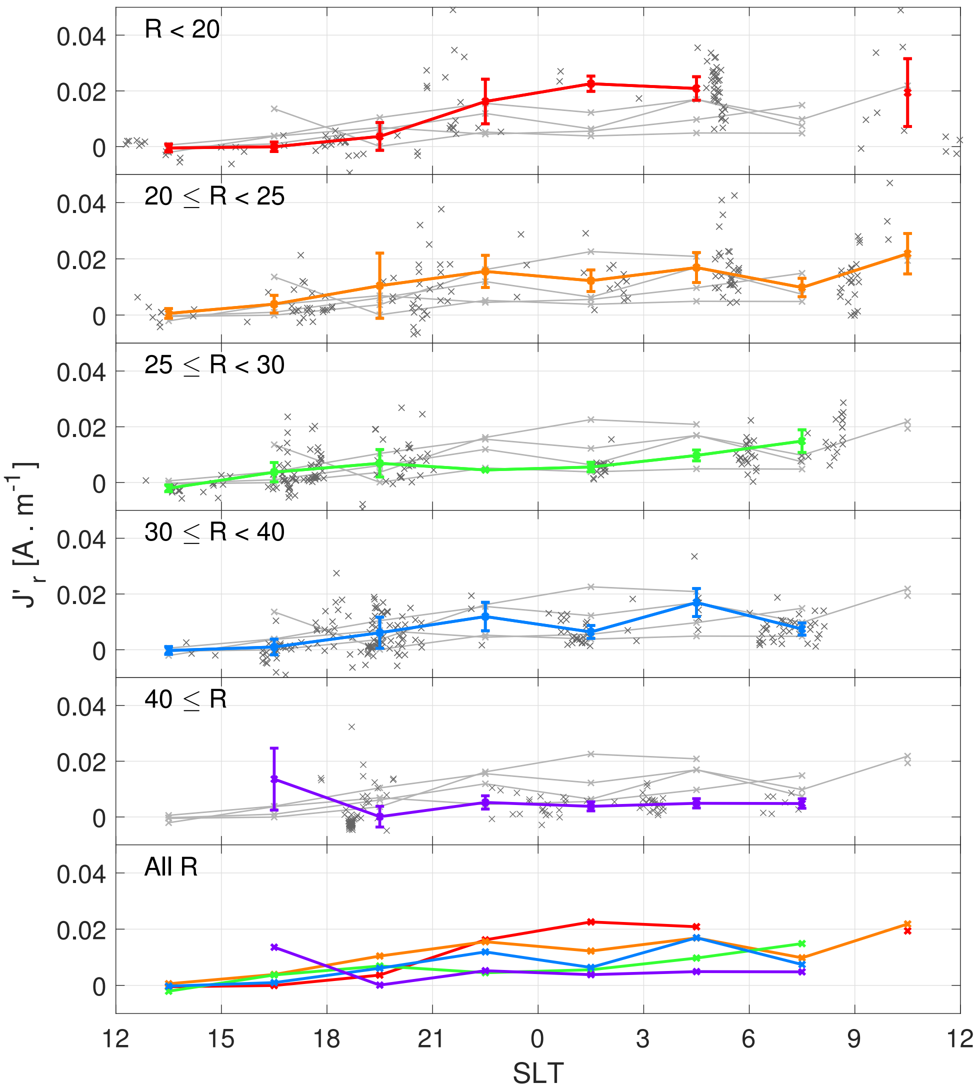

314 **Figure 6.** Figure showing the radial HICD for various radial distances. The top five panels show the values (grey crosses) of radial HICD measured along with the mean of each SLT bin connected with the standard deviation of each bin in colour. The other lines are shown in pale grey as a comparison and the bottom panel shows all of the plots together without standard deviation bars to show to radial relationship.

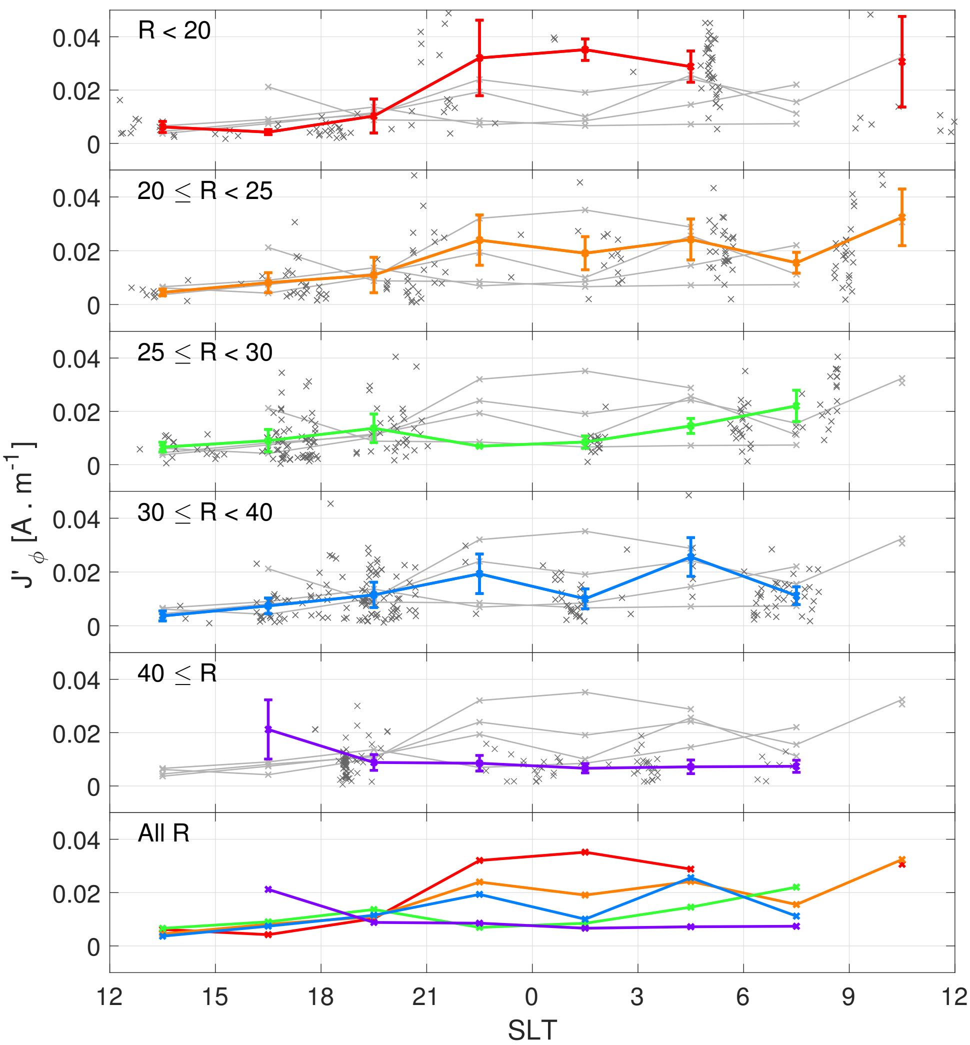

318 **Figure 7.** Figure showing the azimuthal HICD for various radial distances. The top five panels show the
319 values (grey crosses) of azimuthal HICD measured along with the mean of each SLT bin connected with
320 the standard deviation of each bin in colour. The other lines are shown in pale grey as a comparison and the
321 bottom panel shows all of the plots together without standard deviation bars to show to radial relationship.